

Sliding friction and superlubricity of colloidal AFM probes coated by tribo-induced graphitic transfer layers

Renato Buzio^{*,†}, Andrea Gerbi[†], Cristina Bernini[†], Luca Repetto[‡], Andrea Vanossi^{§,⊥}

[†]CNR-SPIN, C.so F.M. Perrone 24, 16152 Genova, Italy

[‡]Dipartimento di Fisica, Università degli Studi di Genova, Via Dodecaneso 33, 16146 Genova, Italy

[§]CNR-IOM Democritos National Simulation Center, Via Bonomea 265, 34136 Trieste, Italy

[⊥]International School for Advanced Studies (SISSA), Via Bonomea 265, 34136 Trieste, Italy

Colloidal probe Atomic Force Microscopy (AFM) allows to explore sliding friction phenomena in graphite contacts of nominal lateral size up to hundreds of nanometers. It is known that contact formation involves tribo-induced material transfer of graphite flakes from the graphitic substrate to the colloidal probe. In this context, sliding states with nearly-vanishing friction, i.e. superlubricity, may set in. A comprehensive investigation of the transfer layer properties is mandatory to ascertain the origin of superlubricity. Here we explore the friction response of micrometric beads, of different size and pristine surface roughness, sliding on graphite under ambient conditions. We show that such tribosystems undergo a robust transition towards a low-adhesion, low-friction state dominated by mechanical interactions at one dominant tribo-induced nanocontact. Friction force spectroscopy reveals that the nanocontact can be superlubric or dissipative, in fact undergoing a load-driven transition from dissipative stick-slip to continuous superlubric sliding. This behavior is excellently described by the thermally-activated, single-asperity Prandtl-Tomlinson model. Our results indicate that upon formation of the transfer layer, friction depends on the energy landscape experienced by the topographically-highest tribo-induced nanoasperity. Consistently we find larger dissipation when the tribo-induced nanoasperity is sled against surfaces with higher atomic corrugation than graphite, like MoS₂ and WS₂, in prototypical Van der Waals layered hetero-junctions.

INTRODUCTION

Superlubricity loosely refers to situations in which sliding friction vanishes or very nearly vanishes.¹ For graphitic systems, such as graphite and graphene flakes,²⁻⁶ characterized by weak dispersive interactions, superlubricity develops because of the presence of atomically flat shear planes at the contacting interfaces. In typical experimental setups the superlubric regime emerges after the built-in of tribo-induced material, called transfer layer (TL), from the graphite substrate onto the sliding countersurface.^{7,2,8,9} Nanosized flakes forming the graphitic TL,¹⁰ similarly to other 2D materials (e.g. MoS₂),¹¹ are thought to randomly arrange in misaligned configurations, providing an effective cancellation of lateral force components via interface incommensurability (structural lubricity), which might lead to friction coefficients as low as 10^{-3} . In this context, one groundbreaking experiment, dating back to 2004 by Dienwiebel *et al.*,² demonstrated interlayer registry-dependent friction in a nanoscale contact between a graphite flake attached to an AFM tip and a pristine graphite substrate. Specifically, it was shown that when the two contacting atomic lattices are aligned in registry high interlayer friction values are measured, whereas friction practically vanishes for orientationally misaligned configurations. Structural lubricity was later documented in other graphitic nanosystems (e.g. nanoribbons and nanotubes)¹² and is nowadays actively investigated in Van der Waals layered hetero-junctions, where the lattice mismatch between graphite and other crystalline counter-surfaces might help to realize stable incommensurate sliding.¹³⁻¹⁶

Recently, colloidal AFM experiments have addressed the scale up of structural lubricity from nanoscale to mesoscale. It has been shown that when ideally smooth silica microspheres (nominal curvature radius $R \sim 10 \mu\text{m}$, surface roughness $\sigma < 2\text{nm}$) are repeatedly rub on Highly Oriented Pyrolytic Graphite (HOPG) under ambient conditions, the contact may evolve towards a low-adhesion, low-friction state due to the formation of a graphitic TL on the beads' surface.^{10,17} Few-layer and multilayer graphene flakes, generated by fracture and peeling of graphite at the surface-exposed step edges, do form the TL. Flakes

mostly retain the crystalline phase¹⁰ and lubricity¹⁷ of bulk graphite, and ultra-small friction coefficients ($\lesssim 10^{-3}$) have been measured. To ascertain the microscopic mechanisms governing superlubricity in such case, the contact mechanics at the TL/HOPG interface needs to be elucidated. Early reports¹⁰ speculated that lubricity relies on the pristine surface roughness of the colloidal probe, that incorporates nanoasperities covered by randomly oriented graphene nanopatches. This implies a multi-asperity contact mechanics, exploiting the cumulative effect of many incommensurate nanocontacts. However, large-scale simulations for the contact of rough spheres reveal that an ubiquitous single-asperity regime virtually emerges at any contact interface under low-loads conditions.¹⁸ This is because at the lowest loads the interfacial mechanics of a rigid rough microparticle (pressed against an ideally-smooth surface) is governed by the first (nano)asperity that touches. Recently, we found that single-asperity contact mechanics – involving one dominant graphitic nanocontact – provides a comprehensive explanation of the friction behavior and superlubricity displayed by smooth silica microspheres ($R \sim 12 \mu\text{m}$, $\sigma < 1 \text{nm}$) sliding on graphite.¹⁷ There is certainly need to better clarify through experiments how common microparticles' properties, such as their size and roughness, affect the formation of the superlubric TL. In this paper we go beyond the case of an ideally smooth silica microparticle,^{10,17,19} by considering a representative set of nominally-rigid colloidal probes having different curvature radius ($R \sim 2 - 25 \mu\text{m}$) and pristine surface roughness ($\sigma \sim 0.5 - 15 \text{nm}$). We complement conventional AFM force spectroscopy with knowledge derived from the TL morphology and atomic-scale friction force spectroscopy. We show that the phenomenology underpinning the appearance of superlubricity is robust against variations of the microparticle size and pristine surface roughness. Indeed, it is the roughness associated to the tribo-induced TL that makes the TL/HOPG contact nanoscopic in size, so that superlubricity may appear depending on the specific energy landscape experienced by the topographically-highest tribo-induced nanoasperity. Thanks also to numerical modeling, we attest the excellent agreement of atomic-scale friction data with the thermally-activated, single-asperity Prandtl-Tomlinson model. Noteworthy, these findings appear highly relevant to ascertain the origin of interfacial friction in prototypical Van der Waals hetero-junctions between the tribo-induced graphitic TLs and other bulk layered materials. In this respect

the single-asperity Prandtl-Tomlinson model offers clear pathways to predict dissipation of hetero-contacts with typical transition metal dichalcogenides, like MoS₂, WS₂ and NbSe₂ single-crystal substrates. Also, results can provide a better comprehension of the mechanisms that assist the emergence of dry superlubricity by carbon-based additives.^{5,20,21}

EXPERIMENTAL SECTION

Colloidal probes and friction experiments. Colloidal AFM probes of diameter $\leq 11\mu\text{m}$ were commercially-available products (Novascan Technologies). According to the manufacturer, they consisted of rectangular shaped cantilevers with borosilicate glass (BG) beads of diameter $\sim 5\mu\text{m}$ (cantilever elastic constant $k_c \sim 4.5\text{N/m}$) and $\sim 11\mu\text{m}$ ($k_c \sim 14\text{N/m}$) respectively. We prepared larger colloidal probes using a micromanipulation stage (Newport M-460A-XYZ 3 axis stage equipped with SM/DM-13 differential screws) coupled with an optical microscope²². We glued monodisperse microspheres of silica (SiO₂) (MicroParticles GmbH) or titanium (Ti) (Alfa Aesar GmbH)²³ to rectangular Si cantilevers (MikroMasch HQ:NSC35/tipless, NSC12/tipless) using molten Shell Epikote resin dispensed on heated probes (heating temperature $\sim 140^\circ\text{C}$, 50W heater cartridge controlled by a Lake Shore 335 temperature controller). The elastic constant of each cantilever was measured by Sader's method²⁴ before the bead attachment, and was in the range $k_c \sim 2.5 - 5.8\text{N/m}$. The surface morphology of the beads was routinely characterized in the course of experiments by reverse AFM imaging on a spiked grating (Tipsnano TGT01). Additionally, SEM imaging of the beads' surface was completed under a 1kV acceleration voltage (CrossBeam 1540 XB by Zeiss). Figure 1 shows the pristine surface morphology of the four representative probes used in the present study. For the BG beads (Figure 1a,b) their cross sections are satisfyingly fitted by circular fits, with curvature radii ($R = 1.9\mu\text{m}$ and $4.1\mu\text{m}$) slightly smaller than those declared by the manufacturer. The surface morphology of the larger BG bead is indeed far from homogeneous, as several isolated bumps – from tens to hundreds of nanometers in size – are superimposed over the bead circular profile. Surface roughness for the BG probes, evaluated after

subtraction of the spherical shape, is $\sigma \sim 4\text{nm}$ ($R = 1.9\mu\text{m}$) and $\sigma \sim 15\text{nm}$ ($R = 4.1\mu\text{m}$) on areas of $\sim 1\mu\text{m}^2$. On the other hand, the pristine SiO_2 colloidal probe ($R = 11.0\mu\text{m}$) is a nearly-ideal smooth sphere, with surface roughness $\sigma \sim 0.5\text{nm}$ (Figure 1c). Finally, the surface of the Ti colloidal probe ($R = 25.0\mu\text{m}$) appears rather irregular, with nanometric scratches and bumps and surface roughness $\sigma \sim 6\text{nm}$ (Figure 1d).

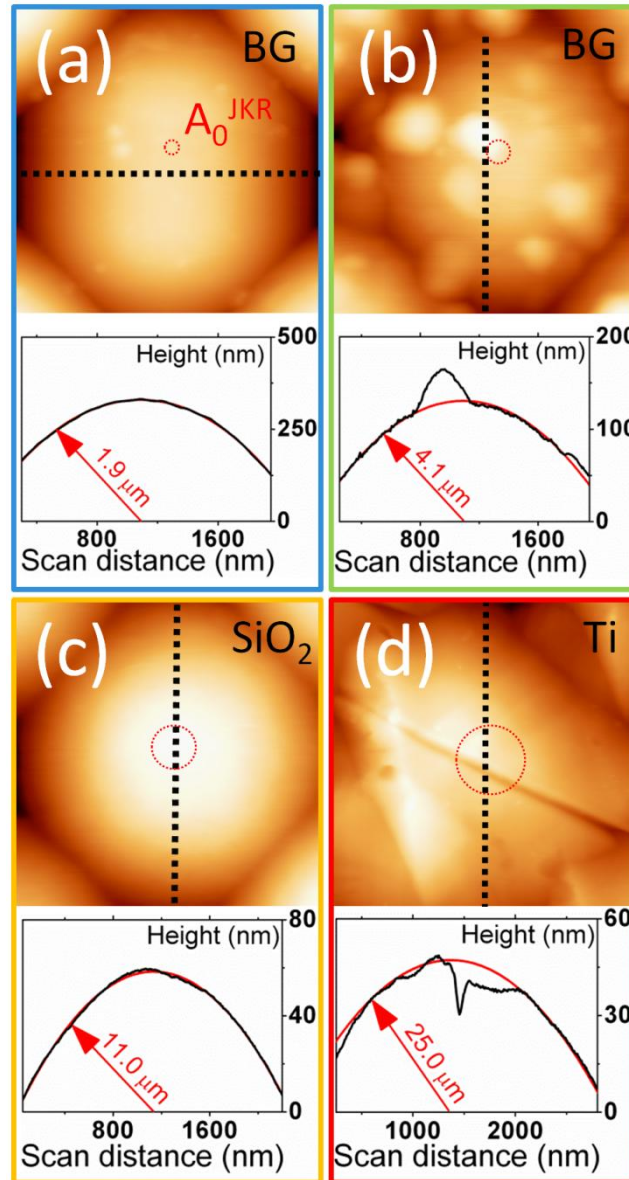


Figure 1. (a),(b) Reverse AFM topographies of two BG colloidal probes in their pristine state. Bottom panels show the cross-sectional height (black line), the circular fit (red line) and the estimated curvature radius R . (c) As in (a), for a SiO_2 probe. (d) As in (a), for a Ti probe. Red dotted circles in (a-d) show how the zero-load contact area A_0^{JKR} scales with R (see text).

Beads of different size and degree of surface roughness were intentionally chosen to evaluate their impact on TL formation and superlubricity. According to Johnsons-Kendall-Roberts JKR theory (see Figure S1 of Supporting Information), ideally-smooth spheres with the same radius R of the colloidal probes span a zero-load Hertzian contact area A_0^{JKR} ranging between $\sim 8 \times 10^3 \text{ nm}^2$ and $\sim 2 \times 10^5 \text{ nm}^2$ when placed in contact with graphite. This corresponds to a mesoscopic contact diameter $\sim 100 \text{ nm} - 500 \text{ nm}$ (see red dotted circles in Figure 1). We expect that both the BG/HOPG ($R = 1.9 \mu\text{m}$) and the SiO_2 /HOPG interfaces should have zero-load contact areas close to A_0^{JKR} , in view of the small pristine roughness. On the contrary A_0^{JKR} only provides an upper limit to the real contact area at the (rougher) BG/HOPG ($R = 4.1 \mu\text{m}$) and Ti/HOPG interfaces. Again, these differences offer the possibility to address the contact formation under different working conditions.

Sliding friction experiments were performed under ambient conditions (relative humidity $\text{RH} \sim 40 - 60\%$, temperature $T = 23 \pm 3^\circ\text{C}$) by means of a commercial AFM operated in contact mode (Solver P47-PRO by NT-MDT, Russia). The normal force F_N and the lateral force F_L were calibrated as reported elsewhere.¹⁷ Friction force *vs* normal load (F_f *vs* F_N) characteristics were obtained by decreasing F_N every ten lines from a large value ($F_N \sim 400 - 700 \text{ nN}$) to the pull-off point; the corresponding lateral forces (calculated from the difference between forward and backward scans) were averaged in between the normal force F_N jump to produce one data point.^{25,20} The F_f *vs* F_N curves were acquired over atomically-flat areas free of atomic steps (scan range from $5 \times 5 \text{ nm}^2$ up to $300 \times 300 \text{ nm}^2$). Friction maps were analyzed with National Instruments LabView and they were displayed using WSXM.²⁶ Normal force *vs* displacement curves were obtained by recording the cantilever deflection (i.e. the normal force F_N), while ramping the relative distance between the tip and sample, and they were transformed into normal force *vs* distance (F_N *vs* D) curves by assigning $D = 0$ to the region where normal force becomes strongly repulsive.^{20,27} Adhesion force was estimated at the pull-off point.

For HOPG, we used a square substrate of grade ZYB (MikroMasch), with the armchair and zigzag crystallographic directions of the (0001) HOPG surface parallel to the edges of the square.²⁸ Graphite was cleaved by adhesive tape in ambient air prior to friction measurements. The substrate was mounted onto

the sample stage with a fixed orientation, that corresponded to a sliding direction slightly off ($\leq 10^\circ$) the armchair crystallographic direction. Commercially-available crystals of 2H-MoS₂ and 2H-WS₂ (from HQ Graphene), together with a laboratory-grown 2H-NbSe₂ single-crystal sample (see Figure S2 for the typical surface topography of this sample),²⁹ were also used for friction measurements after being cleaved by adhesive tape in air. The cleaved surfaces usually showed atomically-flat terraces extending several micrometers.

Analysis and simulations of atomic-scale friction data. Experimental atomic-scale friction maps were analyzed in the framework of the one-dimensional Prandtl-Tomlinson (PT) single-asperity model.³⁰ In the PT modeling approach, a single point-like asperity (mimicking the AFM tip) is elastically driven over an on-site (sinusoidal) potential of amplitude E_0 and lattice spacing a (the corrugated substrate) via a pulling spring, connecting the position of the probing tip itself to an external stage (the AFM support) moving at constant speed. The spring value k , in the PT description, represents an effective system stiffness, combining both the torsional features of the cantilever and the mechanical properties of the interface contact. The PT model describes two distinct dynamical regimes for the tip motion depending on the Tomlinson parameter η , representing the ratio between the corrugation and the effective elastic energy. When $\eta \leq 1$ the system total potential exhibits only one minimum and the sliding motion is smooth with vanishing energy dissipation; for $\eta > 1$, two or more potential minima appear in the energetic landscape and the dynamics becomes intermittent and characterized by dissipative stick-slip transitions. Similarly to^{30,31}, we evaluated E_0 , η and k as a function of applied load. In short, at each normal load F_N , we selected lateral force traces with periodicity a ($\sim 0.21 - 0.25$ nm for HOPG; $\sim 0.29 - 0.32$ nm for MoS₂ and WS₂), corresponding to trajectories characterized by individual slip jumps approximately along the zigzag crystallographic direction. Frictional traces exhibiting different slips were disregarded. For each selected force profile, the corrugation amplitude E_0 , the Tomlinson parameter η and the effective contact stiffness k were estimated as:

$$E_0 = \frac{aF_{L,max}}{\pi} \quad (1)$$

$$\eta = \frac{2\pi F_{L,max}}{ak_{exp}} - 1 \quad (2)$$

$$k = \frac{\eta+1}{\eta} k_{exp} \quad (3)$$

where $F_{L,max}$, a and k_{exp} are, respectively, the highest sampled local force maxima, the slip distance, and the lateral force slope at the initial stick phase. Experimentally, for each applied load F_N , the statistically meaningful mean values of E_0 , k and η were obtained by averaging over several lateral friction traces.

Theoretically, friction *vs* displacement profiles to be compared with experiments, were extracted by integrating *via* a 4th-order Runge-Kutta algorithm the underdamped Langevin equation for the PT model:

$$m\ddot{x} + m\gamma\dot{x} = -\frac{\partial V(x,t)}{\partial x} + \xi(t) \quad (4)$$

where the potential energy of the system $V(x, t)$ reads:

$$V(x, t) \equiv -\frac{E_0}{2} \cos\left(\frac{2\pi x}{a}\right) + \frac{1}{2}k(vt - x)^2 \quad (5)$$

The instantaneous lateral friction trace was simply evaluated by considering the time-dependent elongation of the pulling spring:

$$F_L = k(vt - x) \quad (6)$$

For the effective tip mass we used multiples of $m_0 = 1 \times 10^{-12}$ Kg, whereas the Langevin damping $\gamma = 2\sqrt{k m}$ was chosen to reproduce experimental force traces. The thermal noise term $\xi(t)$ satisfies the

fluctuation-dissipation theorem: $\langle \xi(t)\xi(t') \rangle = 2m\gamma k_B T \delta(t - t')$. Temperature $T = 296\text{K}$, spring stiffness k and sliding velocity $v = 30\text{nm/s}$ where chosen to match AFM experiments.

RESULTS AND DISCUSSION

TL formation from nanoscale force spectroscopy. According to previous studies,^{10,17,19} the ‘ultralow-friction’ interface results from tribo-induced material transfer from the graphitic substrate to the sliding countersurface. We enabled material transfer by driving colloidal probes over HOPG with the sliding direction perpendicular to the local orientation of the surface steps (scan areas from $1 \times 1\mu\text{m}^2$ to $8 \times 8\mu\text{m}^2$, velocity $\sim 1 - 50\mu\text{m/s}$). This choice in fact aids material transfer from HOPG to the AFM probe.¹⁹ As resumed in Figure 2, the process of TL formation showed qualitatively similar features for all beads. Figure 2a reports the evolution of the friction force for each probe, displayed over an arbitrary sliding distance of $\sim 2.5 \times 10^4 \mu\text{m}$. One observes that initially, in the absence of the TL, friction force fluctuates randomly in the range of several hundreds of nN (high-friction state). As scanning progresses however, a permanent drop of the friction force to a few nN takes place (low-friction state). The fall of friction force is a typical signature for the formation of a graphitic TL. Below we use TL/HOPG to indicate the TL-mediated contact between each colloidal probe and HOPG. We note that the sliding distance to achieve the ultralow-friction TL/HOPG interface varied greatly from probe to probe.^{10,17} This reflects the random character of interfacial wear and tribotransfer processes at the base of the TL formation.¹⁷ It is known that nanoscale asperities superimposed on the beads surface can initiate fracture and peeling of graphite at the surface exposed step edges at lateral forces above $F_L \sim 50\text{nN}$.³² Therefore, wear is likely to take place for the pristine beads ($F_L \gg 100\text{nN}$) and flakes can be tribotransferred from HOPG to the contact area. Figure 2b reveals that the TL formation was also accompanied by a simultaneous drop of contact adhesion. Specifically the large adhesion at the pristine interfaces, $F_A \sim 1.7 - 2.2\mu\text{N}$ for $R \geq 11\mu\text{m}$ and $F_A \sim 250 - 500\text{nN}$ for $R \leq 4.1\mu\text{m}$, was reduced to $F_{A,TL} < 200\text{nN}$ for the

TL/HOPG interface regardless of the probe radius R . The absence of a trivial scaling $F_{A,TL} \propto R$ after TL formation signals that a few random morphological features likely control contact mechanics³³ (see also next section). Furthermore, the abrupt snap-off-contact for the TL/HOPG interface supports the picture that contact forces are governed by one dominant contact.³⁴ Figure 2c shows a selected ensemble of F_f vs F_N characteristics acquired over atomically-flat areas of graphite (from $200 \times 200\text{nm}^2$ to $500 \times 500\text{nm}^2$) for the TL/HOPG contacts. Linear regression gives $\mu \sim 0.001$, which agrees with previous reports³⁵ and attests that an ‘ultralow-friction’ interface is achieved for each colloidal probe.

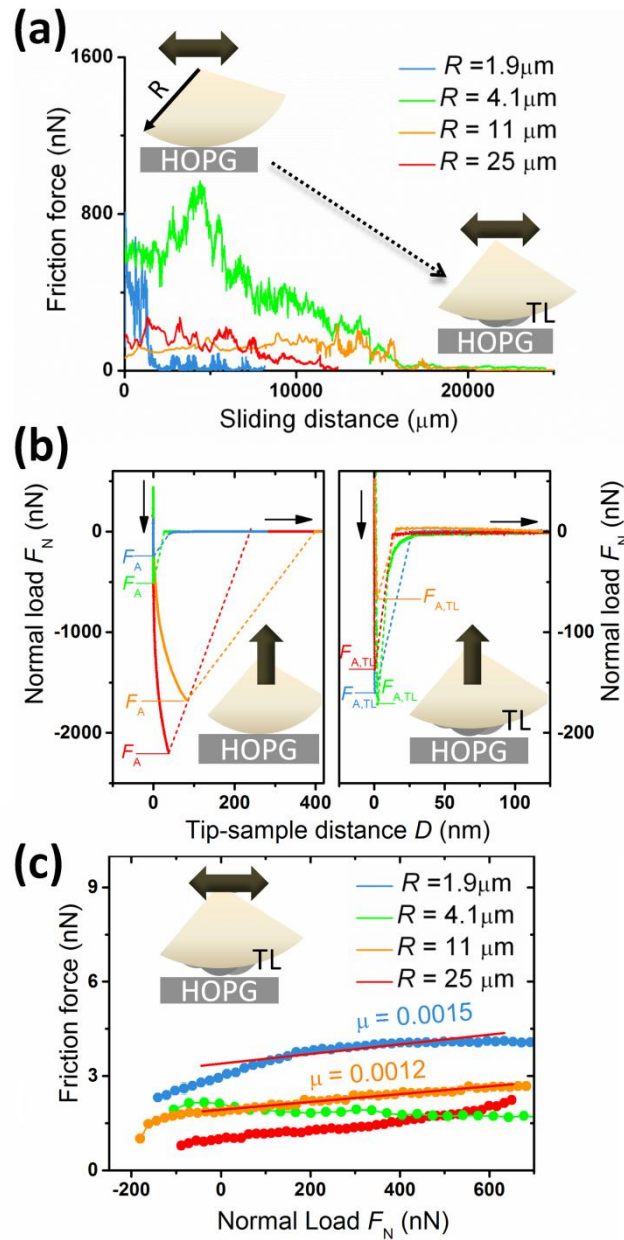


Figure 2. (a) Friction force vs sliding distance, showing the transition from a ‘high-friction’ state proper of the pristine colloidal probes to an ‘ultralow-friction’ state attesting the TL formation. (b) Normal load vs distance curves for the pristine

contacts (left) and for the TL/HOPG contacts (right; color code as in (a)). (c) Load-dependent friction characteristics for the ultralow-friction TL/HOPG contacts.

In the next section we show that the TL is rough on the nanometers scale, and in fact it leads to a substantial increase of the surface roughness σ for each probe. Therefore, in line with our previous AFM experiments using ideally smooth colloidal probes,¹⁷ we claim that the main effect of the TL is to turn the nominally mesoscopic contact area A_0^{JKR} into a nanoscopic one. The roughness-induced decrease of the real contact area readily gives the breakdown of the friction force F_f , as the interfacial shear stress with graphite is known to not vary substantially with contact pressure.²⁰ Also, the capillary adhesion - that typically dominates over van der Waals forces under ambient conditions³⁶ - decreases if interfacial roughness overcomes the Kelvin length scale of capillary condensation $\lambda_K = 0.52\text{nm}$. Thus the TL roughness is expected to greatly suppress the contact adhesion too, i.e. $F_{A,TL} \ll F_A$.

TL morphology and asperity-mediated contact. We routinely characterized the evolution of the surface morphology of the colloidal beads during sliding friction measurements by means of reverse AFM imaging.³⁷ According to Figure 3, the TL consists of flakes of lateral size $\sim 50 - 100\text{nm}$, clustered within the contact region of each bead. Cross sections attest that the flakes rise tens of nanometers away from the beads' profile ($\sim 5 - 50\text{nm}$), in fact representing isolated asperities. Additionally, we confirmed *via* reverse friction maps the ultralow friction response of such flakes (not shown),¹⁷ this being an indication of their graphitic nature. Hence, after TL formation, the beads surface is covered by superlubric nanoasperities. Such conclusions are well corroborated by high-resolution SEM micrographs of the graphitic flakes (see Figure S3).

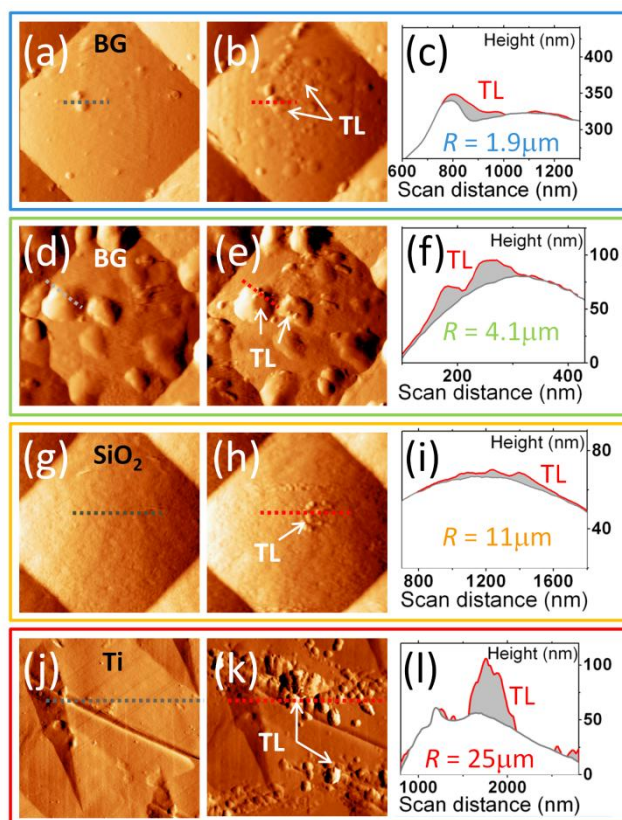


Figure 3. Representative AFM maps (error signals) comparing the surface of each bead respectively before ((a),(d),(g),(j)) and after ((b),(e),(h),(k)) the TL formation (curvature radius R increases from top to bottom). Cross sectional heights ((c),(f),(i),(l)) - taken along the dashed lines in the AFM maps - shown that the TL originates several protruding nanoasperities, or it covers the already-existing ones.

Figure 4a documents the systematic increase of the beads' morphological roughness within the contact region after the TL formation. In particular, for the smooth SiO_2 bead ($R = 11\mu\text{m}$) roughness increases from $\sigma \sim 0.5\text{nm}$ (without TL) to $\sigma_{\text{TL}} \sim 2\text{nm}$ (with TL). Importantly, this value agrees with the thickness of individual nanoflakes imaged by AFM onto worn graphite areas.¹⁷ Also, it agrees with the 2.3nm –thick TL measured by Li *et al.* by means of high-resolution electron microscopy, in colloidal probe AFM experiments using smooth silica beads.¹⁰

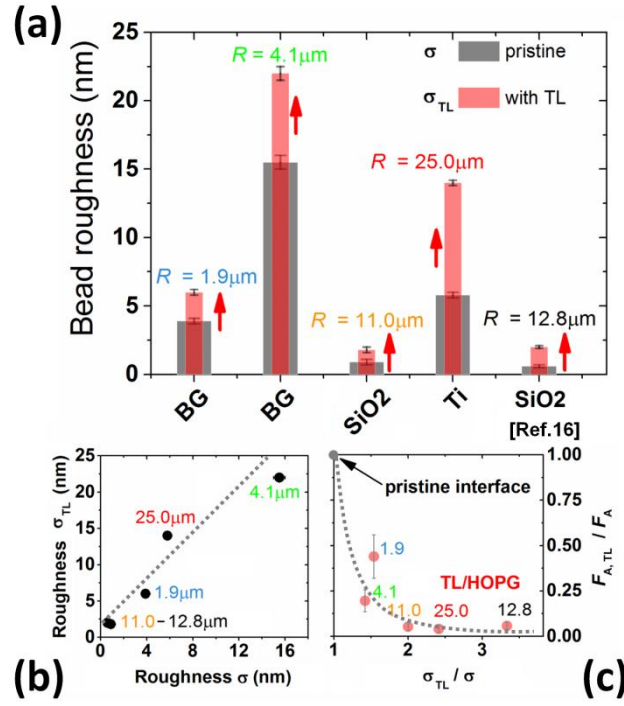


Figure 4. (a) Surface roughness measured within the contact region, respectively before (σ) and after (σ_{TL}) the TL formation: roughness increases for each colloidal bead (red arrows). Data from¹⁷ are added for comparison. (b) Plot of σ_{TL} vs σ , indicating good correlation of the two quantities (dash line is a guide to eye). (c) Plot of the normalized adhesion vs normalized roughness, showing the existence of a ‘minimum adhesion plateau’ for $\sigma_{TL} \sim 2\sigma$ ($\sigma_{TL}/\sigma = 1$ corresponds to pristine interfaces; dash line is a guide to eye).

The systematic increase of the roughness σ_{TL} with the pristine roughness σ , resumed in Figure 4b, reflects the fact that the tribo-transferred flakes preferentially form new asperities rather than being incorporated within the already-existing beads’ surface valleys, so that their overall effect is to enhance topographical variations within the contact region. This readily emerges by inspection of Figures 3d-e,j-k.

As mentioned in the previous section, the main role of the TL roughness is to decrease the real contact area between the beads and HOPG. As a result, both the pull-off (adhesive) force and the friction force are drastically reduced. The effects of surface roughness on adhesion have been studied extensively in particle technology, adhesion science, and fundamental physics and chemistry.³⁸ In the context of colloidal probe AFM experiments, the breakdown of adhesion upon increase of interfacial roughness is well documented for nominally rigid interfaces.^{33,34,39,40} Adhesion reduction has been reported also when interfacial nanoasperities originate from accumulated wear debris,⁴¹ in a situation similar to the tribo-

transferred-flakes case. Noteworthy, a plot of the normalized adhesion ($F_{A,TL}/F_A$) vs normalized roughness (σ_{TL}/σ) (Figure 4c) indicates the existence of a ‘minimum adhesion plateau’ for the TL/HOPG interface (for $\sigma_{TL} \gtrsim 2\sigma$), in analogy with similar trends found for other systems.^{33,34,40} This plateau corresponds to the adhesion experienced within a graphitic nanosized contact spot (e.g. see¹⁷ for a simplified calculation of $F_{A,TL}$ under 40-60% RH conditions).

We note that the occurrence of several superlubric asperities over the beads’ surface does not necessarily imply a multi-asperity contact regime. To clarify this issue we observe that the TL formation was accompanied also by emergence of multiple-tip effects (Figure S4). These arise whenever the graphite roughness, associated to airborne adsorbates or to surface steps, has an aspect ratio comparable to the TL roughness.⁴² Topographies, in such case, display repetitive patterns revealing the arrangement of those asperities affecting contact mechanics. On the contrary, normal and shear forces are likely supported by one asperity only (i.e. the most prominent one) when the probe slides over atomically-flat graphite.¹⁷ This picture appears reasonable also with respect to scaling arguments derived from large scale molecular simulations.^{18,40} Briefly, these indicate that the contact between a self-affine rough microsphere and a flat substrate evolves with the ratio F_N/N_C , where the critical load $N_C = (9\pi^3/16) E^* R^2 (h'_{rms}/\kappa)^3$ depends on material and geometrical parameters (E^* is the contact modulus, R is the sphere radius, h'_{rms} is the dimensionless root mean square topographical slope and $1/\kappa$ is a dimensionless constant). According to the model of the nonadhesive hard-wall limit, for $F_N/N_C \gtrsim 1$ contact mechanics is single-asperity and dominated by the microscopic sphere radius R , for $10^{-4} \lesssim F_N/N_C < 1$ a multi-asperity regime takes place due to a statistical number of nanometric contact spots, whereas a crossover to a single-asperity regime (governed by the first nanoasperity that touches) occurs for $F_N/N_C < 10^{-4}$. In the present case one gets the estimate $N_C \sim 120 - 210 \mu\text{N}$ (with $R = 1.9 \mu\text{m}$ and $11 \mu\text{m}$, see Figure S5). This suggest that the TL/HOPG interface is nearby the cross-over from multi-asperity to single-asperity for $F_N \sim 100 \text{nN}$, and it can easily evolve towards a single-asperity nanocontact in the small-loads limit (e.g. $F_N \sim 10 \text{nN}$). Accordingly, neither the curvature radius R nor the pristine surface roughness ($\sigma < \sigma_{TL}$) are expected to significantly impact the TL/HOPG contact mechanics.

Atomic-scale friction and superlubricity of the tribo-induced TL sliding on graphite. Analysis of atomic-scale lateral force maps allowed to characterize the elementary dissipation mechanisms at the TL/HOPG interface. Such maps typically showed stick-slip motion in the normal load range $100\text{nN} \lesssim F_N \lesssim 600\text{nN}$ (Figure 5a). Remarkably, this occurred for all colloidal probes. The ubiquitous presence of stick-slip motion signals the existence of an interlocking mechanism between one dominant TL nanoasperity and the underneath graphite substrate.¹⁷

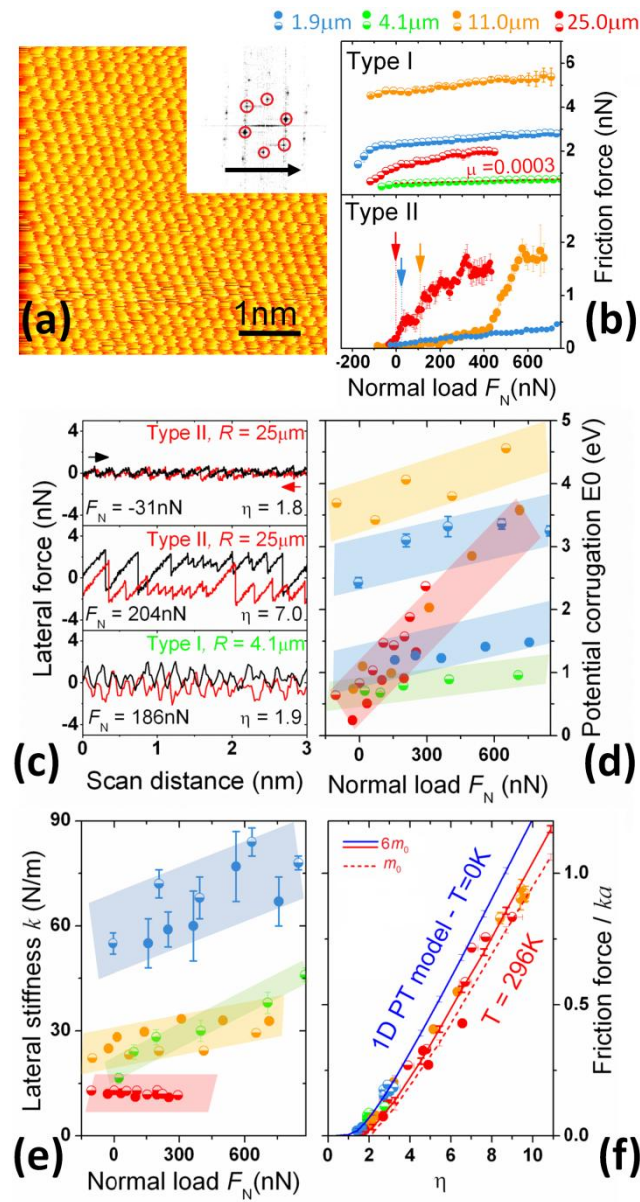


Figure 5 (a) Friction map acquired at the atomic scale ($R = 25\mu\text{m}$); in the inset, 2D FFT with the hexagonal symmetry of the graphite lattice together with the probe sliding direction). (b) Representative set of F_f vs F_N characteristics ($v = 33\text{nm/s}$).

Arrows indicate the critical load for the transition from superlubric sliding to stick-slip in Type II curves (see text). (d) Load-dependent friction loops for some of the friction curve in (b). (d-e) Load-dependent potential corrugation E_0 and contact stiffness k estimated from analysis of curves in (b). (f) Normalized friction force F_f^* vs η and comparison with the 1D PT model ($m_0 = 1 \times 10^{-12}$ Kg; see text).

The F_f vs F_N curves were affected by some variability at the atomic scale. This reflects changes in the fine details of the TL/HOPG contact, taking place during the experiments. Some representative characteristics are reported in Figure 5b, conveniently separated into two groups. On one hand there are curves with a weak dependence on load and finite friction force $F_f \geq 0.5$ nN down the pull-off point ('type I' friction curves). On the other side, there are entirely different characteristics showing vanishing friction at the lowest loads and a monotonic increase at some point ('type II' friction curves). Notably, each colloidal probe showed characteristics of both types in the course of the experiments (with the exception of the BG probe with $R = 4.1 \mu\text{m}$, that showed only 'type I' curves). Inspection of friction loops in 'type II' curves (Figure 5c) shows that energy dissipation substantially evolves with the normal load F_N , from nearly-frictionless continuous sliding (e.g. at $F_N = -31$ nN) to highly-dissipative (single-slip and multi-slip) stick-slip motion ($F_N = 204$ nN); this is not the case for type I curves, which did not show continuous superlubric sliding even at the largest tensile loads. Qualitatively this phenomenology agrees with atomic-friction experiments conducted on graphite by means of sharp AFM tips^{43,44} and suggests to use the PT model to elucidate the friction behavior of the TL/HOPG interface for each colloidal probe. To this end, we estimated the contact parameters E_0 , k and η of the PT model as a function of F_N . The analysis was carried out for each F_f vs F_N characteristic of Figure 5b. Results are summarized in Figure 5d-f. For each colloidal probe, the potential corrugation E_0 increases with F_N (Figure 5d) and assumes the smallest values for 'type II' curves, whereas higher barriers are systematically associated to 'type I' characteristics. For each probe, 'type I' and 'type II' curves have comparable values of the lateral stiffness k (Figure 5e). This analysis allows mapping different F_f vs F_N curves into the adimensional scaling F_f^* vs η , where $F_f^* \equiv F_f/ak$ is the normalized friction force. In this

way it turns out that all the experimental F_f vs F_N characteristics follow reasonably well the thermally-activated PT model (Figure 5f). Notably, the model predicts a friction force F_f^* systematically smaller than for the athermal ($T = 0\text{K}$) case, as thermal energy do assists the contact asperity of the TL to jump from one minimum of the potential to the next.^{31,45} We thus conclude that small (unpredictable) variations of the TL/HOPG contact move the tribosystem in different positions of the F_f^* vs η plot. In particular, ‘type II’ curves mainly populate the small dissipation region $1.7 \leq \eta \leq 6$. In this region, the contact transitions from continuous superlubric sliding to dissipative stick-slip. As F_N increases the energy barrier E_0 increases faster than the contact stiffness k (Figure 5d,e), so that the Tomlinson parameter $\eta \propto E_0/k$ grows with F_N , causing the transition from continuous sliding to a stick-slip mode.⁴⁴ On the other hand, curves of ‘type I’ populate mostly the region $\eta > 6$, where the TL/HOPG contact dissipates mechanical energy only by stick-slip instabilities.⁴⁴

In the previous study¹⁷ on ideally smooth silica beads, we already pointed-out the evocative correspondence between the phenomenology depicted in Figure 5 and friction duality, i.e. the existence of two distinct regimes of finite and vanishing friction, observed respectively in single-asperity AFM experiments⁴⁶ and nanoparticles manipulation experiments⁴⁷ on HOPG. In such reports vanishing friction was attributed to lattice mismatch within the contact area, while finite friction was ascribed to some pinning source, like interfacial defects⁴⁸ or airborne contamination. In line with such reasoning, the ‘type II’ behavior in Figure 5b likely reflects structural lubricity (i.e. in-plane misalignment) for a tribo-induced flake with respect to graphite, holding up to a critical normal force value where dissipative stick-slip sets in. Such threshold can be tensile ($F_N < 0$) or compressive ($F_N > 0$). In the last case it agrees with the $\sim 1 - 40\text{nN}$ found for nanosized contacts.^{30,43,49,50} In turn, the load-driven transition from superlubric sliding to stick-slip motion can reflect the progressive emergence of contact pinning effects. At this level of discussion, one can ascribe pinning to an increase of the degree of interfacial commensurability, e.g. due to small (reversible) in-plane rotations of the tribotransferred flake bearing contact,³¹ or to load-induced pinning effects at the contact edges.⁵¹ Such effects might explain both the monotonic rise of friction for the ultralow ‘type II’ F_f vs F_N curve of Figure 5b above some critical load value. Following

discussion above, ‘type I’ regime could rely on a single-asperity contact fully dominated by pinning effects.

The single-asperity PT phenomenology at atomic scale (Figure 5) indicates that the friction response of the nominally mesoscopic TL/HOPG junction indeed depends on the energy landscape experienced by the topographically-highest tribo-induced nanoasperity. Given the $\sim 50 - 100\text{nm}$ lateral size of the tribo-transferred flakes, such an asperity may involve one or at most a few neighbor flakes. Random interactions of the bead with the HOPG atomic roughness can drive reorganizations of such tribo-induced nanoasperity, that are at the base of the friction fluctuations and variability of experimental friction *vs* load curves documented above.

Friction of the tribo-induced TL sliding on transition metal dichalcogenides. One of the main advantages offered by graphene-coated AFM probes is to enable the investigation of interfacial forces and mechanical dissipation in Van der Waals layered hetero-junctions. In fact, the practical realization of crystalline heterogeneous contacts with 2D materials is crucial to systematically perform fundamental force spectroscopy studies;⁵² also, it is often claimed to be a necessary condition to realize stable incommensurate sliding and – possibly – structural lubricity between mismatched lattices.^{13–16} Quite unexpectedly, however, experiments with graphene-coated probes sled against common transition metal dichalcogenides (e.g. ReS_2 , TaS_2 , MoS_2 , WS_2) attest an increase of the friction force compared to the graphene/HOPG homo-junction.^{53,54} This issue still needs to be fully elucidated, as it demands to rationalize the complex interplay of intrinsic properties (e.g. contact size and elasticity, interfacial corrugation, degree of incommensurability) and extrinsic factors (e.g. interfacial roughness, environmental contaminants, wear). Hereafter we provide deeper insight by probing the frictional response of the graphitic TL sliding against a few transition metal dichalcogenides. We used the following methodology. First, the SiO_2 colloidal bead was sled over HOPG until a superlubric TL/HOPG contact formed. As discussed above, such contact was characterized by $\mu \lesssim 10^{-3}$ and by atomic-scale

continuous sliding for F_N up to a few tens of nN (as for ‘type II’ characteristics in Figure 5b). Then, the very same colloidal probe was retracted from HOPG and immediately engaged on the atomically-smooth surface of a freshly-cleaved bulk crystal, namely MoS_2 (TL/ MoS_2), WS_2 (TL/ WS_2) or NbSe_2 (TL/ NbSe_2). Prior to engage, the probe was carefully located by optical microscopy over a surface region free from visible surface steps; scan area was kept in the sub-micrometric range ($< 500 \times 500 \text{nm}^2$) and prominent interactions of the graphitic TL (covering the SiO_2 bead) with surface steps were avoided. Results – summarized in Figure 6 – confirmed a general robust increase of the friction force at all loads, for each hetero-junction, compared to the superlubric starting condition. Noteworthy, both the single-asperity contact mechanics and the PT model offer pathways to explain the response of such tribosystems.

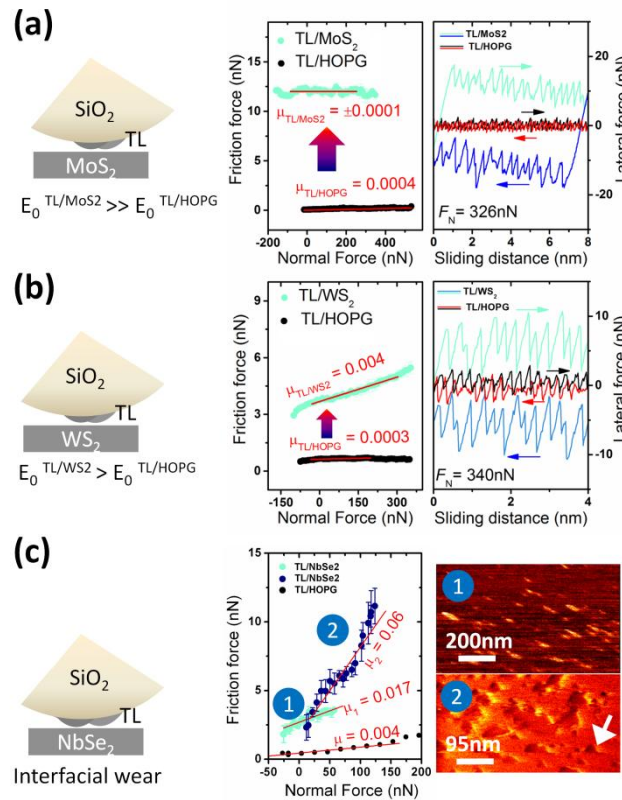


Figure 6. (a) Friction response of the TL/ MoS_2 hetero-junction, resumed in terms of F_f vs F_N curve (left panel) and atomic-scale lateral force traces (right panel). The higher friction of the hetero-junction compared to the TL/HOPG homo-junction reflects the substantial increase of the interfacial corrugation E_0 . (b) As in (a), but for the TL/ WS_2 hetero-junction. (c) Friction response of the TL/ NbSe_2 contact, depicted in terms of F_f vs F_N characteristics (left panel) and AFM maps (right panel). Interfacial wear dictates the friction increase (see text).

For the TL/MoS₂ hetero-junction, friction experiments were carried out up to a few hundreds of nN normal load (Figure 6a), without detection of surface wear. Typically, the friction force was larger ($F_f \sim 12\text{nN}$) than for the TL/HOPG superlubric case ($F_f \sim 0.1 - 0.5\text{nN}$) and was almost load-independent down to the pull-off point ('type I' characteristic). Whereas this would result in a virtually zero friction coefficient ($\mu_{\text{TL/MoS}_2} \sim \pm 10^{-4}$), atomic-scale friction data always indicated the occurrence of significant dissipative stick-slip with periodicity $\sim 0.3\text{nm}$ fitting the MoS₂ atomic lattice. This clearly excludes structural lubricity for our realization of such hetero-junction, involving far less extended tribocontacts if compared to other experimental realizations.¹³ Indeed, according to the single-asperity PT model, dissipative stick-slip results from a Tomlinson parameter $\eta > 1$. This is reasonably expected for the TL/MoS₂ hetero-junction, since a nanoasperity sliding on MoS₂ is known to experience higher energy barriers than on HOPG⁵⁵ so that $\eta \propto E_0$ becomes substantially larger than 1. Consistently we found that the main effect of MoS₂ was to enhance interfacial corrugation from $E_0(\text{TL/HOPG}) \lesssim 0.8\text{eV}$ to $E_0(\text{TL/MoS}_2) \sim 8.0\text{eV}$ that ultimately led to $\eta(\text{TL/MoS}_2) \sim 8$ (see Figure S6). Likewise, for the TL/WS₂ hetero-junction, the friction force was higher ($F_f \sim 3 - 5\text{nN}$) than for the TL/HOPG counterpart ($F_f \sim 0.1 - 0.5\text{nN}$) and dissipative stick-slip with $\sim 0.3\text{nm}$ wavelength occurred (Figure 6b). Again, we found that E_0 increased from $E_0(\text{TL/HOPG}) \sim 1.0\text{eV}$ to $E_0(\text{WS}_2/\text{HOPG}) \sim 4.0\text{eV}$, which ultimately led to $\eta(\text{TL/WS}_2) \sim 6$. The condition $F_f(\text{TL/HOPG}) < F_f(\text{TL/MoS}_2)$ agrees with previous studies on nanosized layered hetero-junctions based on 2D flake-wrapped AFM tips,⁵³ whereas $F_f(\text{TL/WS}_2) < F_f(\text{TL/MoS}_2)$ can be ascribed to the different out-of-plane deformations of the MoS₂ and WS₂ surfaces.⁵⁶

A different situation occurred for the TL/NbSe₂ hetero-junction (Figure 6c). Sliding friction experiments were initially carried out at moderate normal loads ($F_N \leq 50\text{nN}$) and showed an increase of both friction force and friction coefficient ($F_f \sim 1 - 5\text{nN}$; $\mu_1 = 0.017$) compared to the TL/HOPG contact ($F_f \sim 0.1 - 0.5\text{nN}$; $\mu_{\text{TL/HOPG}} \approx 0.004$). Remarkably, the lateral force often showed sharp spikes at randomly-located surface spots (top AFM map in Figure 6c). We realized *a posteriori* that such spikes were precursors of the initiation of atomic surface wear, with the AFM probe sweeping away material fragments from the at the NbSe₂ basal plane. In fact, in a second series of experiments conducted at higher loads ($F_N \leq$

150nN), there was an additional increase of the friction coefficient ($\mu_2 = 0.06 \gg \mu_{\text{TL/HOPG}}$) accompanied by the appearance of characteristic triangular-shaped holes in the investigated area (bottom AFM map in Figure 6c). The mean depth of the holes roughly corresponds to the thickness of one layer of NbSe₂. Wear phenomena on NbSe₂ have been observed previously⁵⁷ in AFM experiments using nanosized tips, with a normal load threshold that can be roughly located between $F_N \sim 25\text{nN}$ ⁵⁷ and $F_N \sim 100\text{nN}$ ^{58,59} according to the actual tip size. Here, the observation of surface wear appears as an obvious consequence of the TL contact mechanics, because an individual tribo-induced nanoasperity mediates the contact between the colloidal bead and NbSe₂ and leads to a high contact pressure exceeding the limit of wearless sliding.

Experiments discussed above, far from being conclusive, strengthen the general correspondence between graphitic tribo-induced TLs and nanocontacts. Results for TL/MoS₂ and TL/WS₂ hetero-interfaces indicate that contact pinning prevails over interfacial incommensurability as soon as graphite is replaced with the other layered bulk substrates. Simulations and tailored experiments appear necessary at this stage to shed more light on the main physical ingredients that govern the evolution of the interfacial corrugation E_0 .

CONCLUSIONS

In this study we addressed the manifestation of ultralow-friction sliding states, including superlubricity, for colloidal AFM probes sliding on graphite under ambient conditions. We have shown that neither the pristine surface roughness nor the curvature radius of the colloidal bead have a major impact on the phenomenology underpinning the appearance of superlubricity. Rather, graphitic flakes are tribo-transferred at the bead-graphite contact region where they form new asperities, so that contact mechanics and mechanical dissipation depend on the details of the topographically-highest, tribo-induced nanoasperity. This clarifies many single-asperity effects encountered in AFM imaging and force spectroscopy, including the dramatic reduction of adhesion and friction forces upon TL formation, the

origin of multiple-tips convolutions effects, and the occurrence of atomic-scale load-controlled transitions from continuous superlubric sliding to stick-slip dissipative motion. Superlubricity strictly occurs only in specific cases, and in the low-load regime. The correspondence of atomic friction data with the well-established PT model, suggests that the friction force ultimately arises from the interplay between interfacial crystalline incommensurability and pinning effects (both at the contact edges or within the contact area). These findings also explain why interfacial friction increases when the tribotransferred flakes are placed in contact with transition metal dichalcogenides, such as MoS₂ and WS₂. Since nanocontacts experience higher sliding barriers on such materials than on graphite, pinning prevails over interfacial incommensurability and a higher dissipation takes place. Our work contributes to the ongoing research on structural lubricity, by offering an original framework of experimental and theoretical evidences suitable to analyse colloidal probe AFM experiments on Van der Waals layered junctions.

ASSOCIATED CONTENT

Contact mechanics calculations with the Johnson-Kendall-Roberts JKR model (Figure S1), AFM/STM topographies of the laboratory-grown 2H-NbSe₂ sample (Figure S2), SEM micrographs of the contact area of each bead (Figure S3), Multiple-tip effects originated by a rough transfer layer (Figure S4), evaluation of the average local slope and critical normal load from AFM topographies (Figure S5), evaluation of atomic-scale contact parameters for sliding hetero-junctions (Figure S6).

AUTHORS INFORMATION

Corresponding Author

* E-mail: renato.buzio@spin.cnr.it (R.B.).

Notes

The authors declare no competing financial interest.

ACKNOWLEDGEMENTS

This work was financially supported by the MIUR PRIN2017 project 20178PZCB5 “UTFROM - Understanding and tuning friction through nanostructure manipulation”. A.V. acknowledges also support from ERC Advanced Grant ULTRADISS, contract No. 86344023.

REFERENCES

- (1) *Superlubricity*; Erdemir, A., Martin, J.-M., Eds.; Elsevier, 2007.
- (2) Dienwiebel, M.; Verhoeven, G. S.; Pradeep, N.; Frenken, J. W. M.; Heimberg, J. A.; Zandbergen, H. W. Superlubricity of Graphite. *Phys. Rev. Lett.* **2004**, 92 (12), 126101.
- (3) Feng, X.; Kwon, S.; Park, J. Y.; Salmeron, M. Superlubric Sliding of Graphene Nanoflakes on Graphene. *ACS Nano* **2013**, 7 (2), 1718–1724.
- (4) Deng, Z.; Klimov, N. N.; Solares, S. D.; Li, T.; Xu, H.; Cannara, R. J. Nanoscale Interfacial Friction and Adhesion on Supported versus Suspended Monolayer and Multilayer Graphene. *Langmuir* **2013**, 29 (1), 235–243.
- (5) Peng, Y.; Wang, Z.; Zou, K. Friction and Wear Properties of Different Types of Graphene Nanosheets as Effective Solid Lubricants. *Langmuir* **2015**, 31 (28), 7782–7791.

- (6) Berman, D.; Erdemir, A.; Sumant, A. V. Approaches for Achieving Superlubricity in Two-Dimensional Materials. *ACS Nano* **2018**, *12* (3), 2122–2137.
- (7) El Mansori, M.; Schmitt, M.; Paulmier, D. Role of Transferred Layers in Friction and Wear for Magnetized Dry Frictional Applications. *Surf. Coatings Technol.* **1998**, *108–109*, 479–483.
- (8) Bowden, F. P.; Tabor, D. *The Friction and Lubrication of Solids*, vol.2; Clarendon Press, Oxford, 1964.
- (9) Li, J.; Ge, X.; Luo, J. Random Occurrence of Macroscale Superlubricity of Graphite Enabled by Tribo-Transfer of Multilayer Graphene Nanoflakes. *Carbon* **2018**, *138*, 154–160.
- (10) Li, J.; Gao, T.; Luo, J. Superlubricity of Graphite Induced by Multiple Transferred Graphene Nanoflakes. *Adv. Sci.* **2018**, *5* (3), 1700616.
- (11) Martin, J. M.; Donnet, C.; Le Mogne, T.; Epicier, T. Superlubricity of Molybdenum Disulphide. *Phys. Rev. B* **1993**, *48* (14), 10583–10586.
- (12) Vanossi, A.; Bechinger, C.; Urbakh, M. Structural Lubricity in Soft and Hard Matter Systems. *Nat. Commun.* **2020**, *11* (1), 1–11.
- (13) Song, Y.; Mandelli, D.; Hod, O.; Urbakh, M.; Ma, M.; Zheng, Q. Robust Microscale Superlubricity in Graphite/hexagonal Boron Nitride Layered Heterojunctions. *Nat. Mater.* **2018**, *17* (10), 894–899.
- (14) Sheehan, P. E.; Lieber, C. M. Friction between van Der Waals Solids during Lattice Directed Sliding. *Nano Lett.* **2017**, *17* (7), 4116–4121.
- (15) Hölscher, H.; Schirmeisen, A.; Schwarz, U. D. Principles of Atomic Friction: From Sticking Atoms to Superlubric Sliding. *Philos. Trans. R. Soc. A Math. Phys. Eng. Sci.* **2008**, *366* (1869), 1383–1404.
- (16) Büch, H.; Rossi, A.; Forti, S.; Convertino, D.; Tozzini, V.; Coletti, C. Erratum to: Superlubricity of Epitaxial Monolayer WS₂ on Graphene. *Nano Res.* **2018**, *11* (11), 5946–5956.
- (17) Buzio, R.; Gerbi, A.; Bernini, C.; Repetto, L.; Vanossi, A. Graphite Superlubricity Enabled by Triboinduced Nanocontacts. *Carbon* **2021**, *184*, 875–890.

- (18) Pastewka, L.; Robbins, M. O. Contact Area of Rough Spheres: Large Scale Simulations and Simple Scaling Laws. *Appl. Phys. Lett.* **2016**, *108* (22).
- (19) Yu, K.; Peng, Y.; Lang, H.; Ding, S.; Huang, Y. Material Transfer Mechanism for Fabrication of Superlubricity Interface by Reciprocating Rubbing on Graphite under High Contact Stress. *Carbon* **2022**, *188*, 420–430.
- (20) Buzio, R.; Gerbi, A.; Uttiya, S.; Bernini, C.; Del Rio Castillo, A. E.; Palazon, F.; Siri, A. S.; Pellegrini, V.; Pellegrino, L.; Bonaccorso, F. Ultralow Friction of Ink-Jet Printed Graphene Flakes. *Nanoscale* **2017**, *9* (22), 7612–7624.
- (21) Le Van Sang; Sugimura, N.; Khajeh, K.; Washizu, H. Solid Lubricants of Combined Graphene and Iron Nanoparticles for Study of Friction and Stability. *Langmuir* **2022**, *38* (5), 1860–1868.
- (22) Buzio, R.; Valbusa, U. Interfacial Stiffness and Adhesion of Randomly Rough Contacts Probed by Elastomer Colloidal AFM Probes. *J. Phys. Condens. Matter* **2008**, *20* (35), 354014.
- (23) Stegemann, B.; Klemm, M.; Horn, S.; Woydt, M. Switching Adhesion Forces by Crossing the Metal–insulator Transition in Magnéli-Type Vanadium Oxide Crystals. *Beilstein J. Nanotechnol.* **2011**, *2*, 59–65.
- (24) Green, C. P.; Lioe, H.; Cleveland, J. P.; Proksch, R.; Mulvaney, P.; Sader, J. E. Normal and Torsional Spring Constants of Atomic Force Microscope Cantilevers. *Rev. Sci. Instrum.* **2004**, *75* (6), 1988–1996.
- (25) Buzio, R.; Toma, A.; Chincarini, A.; de Mongeot, F. B.; Boragno, C.; Valbusa, U. Atomic Force Microscopy and X-Ray Photoelectron Spectroscopy Characterization of Low-Energy Ion Sputtered Mica. *Surf. Sci.* **2007**, *601* (13), 2735–2739.
- (26) Horcas, I.; Fernández, R.; Gómez-Rodríguez, J. M.; Colchero, J.; Gómez-Herrero, J.; Baro, A. M. WSXM: A Software for Scanning Probe Microscopy and a Tool for Nanotechnology. *Rev. Sci. Instrum.* **2007**, *78* (1).
- (27) Buzio, R.; Boragno, C.; Valbusa, U. Friction Laws for Lubricated Nanocontacts. *J. Chem. Phys.* **2006**, *125* (9), 1–8.

- (28) Private Communication by MikroMasch Europe, Operated by NanoAndMore GmbH Steinbuehlstr. 7 35578 Wetzlar Germany.
- (29) Lazard, G.; Mathieu, P.; Plaçais, B.; Mosqueira, J.; Simon, Y.; Guilpin, C.; Vacquier, G. Critical Currents in the Anisotropic Superconductor 2H-NbSe₂: Evidence for an Upper Bound of the Surface Critical-Current Density. *Phys. Rev. B - Condens. Matter Mater. Phys.* **2002**, *65* (6), 645181–645188.
- (30) Socoliuc, A.; Bennewitz, R.; Gnecco, E.; Meyer, E. Transition from Stick-Slip to Continuous Sliding in Atomic Friction: Entering a New Regime of Ultralow Friction. *Phys. Rev. Lett.* **2004**, *92* (13), 134301–1.
- (31) Jinesh, K. B.; Krylov, S. Y.; Valk, H.; Dienwiebel, M.; Frenken, J. W. M. Thermolubricity in Atomic-Scale Friction. *Phys. Rev. B* **2008**, *78* (15), 155440.
- (32) Vasić, B.; Matković, A.; Gajić, R.; Stanković, I. Wear Properties of Graphene Edges Probed by Atomic Force Microscopy Based Lateral Manipulation. *Carbon* **2016**, *107*, 723–732.
- (33) Kumar, A.; Staedler, T.; Jiang, X. Role of Relative Size of Asperities and Adhering Particles on the Adhesion Force. *J. Colloid Interface Sci.* **2013**, *409*, 211–218.
- (34) Ramakrishna, S. N.; Clasohm, L. Y.; Rao, A.; Spencer, N. D. Controlling Adhesion Force by Means of Nanoscale Surface Roughness. *Langmuir* **2011**, *27* (16), 9972–9978.
- (35) Liu, S.; Wang, H.-P.; Xu, Q.; Ma, T.; Yu, G.; Zhang, C.; Geng, D.; Yu, Z.; Zhang, S.; Wang, W.; et al. Robust Microscale Superlubricity under High Contact Pressure Enabled by Graphene-Coated Microsphere. *Nat. Commun.* **2017**, *8* (1), 14029.
- (36) Butt, H.-J.; Kappl, M. Normal Capillary Forces. *Adv. Colloid Interface Sci.* **2009**, *146* (1–2), 48–60.
- (37) Neto, C.; Craig, V. S. J. Colloid Probe Characterization: Radius and Roughness Determination. *Langmuir* **2001**, *17* (7), 2097–2099.
- (38) Persson, B. N. J.; Albohr, O.; Tartaglino, U.; Volokitin, A. I.; Tosatti, E. On the Nature of Surface Roughness with Application to Contact Mechanics, Sealing, Rubber Friction and Adhesion. *J.*

- Phys. Condens. Matter* **2005**, *17* (1), R1–R62.
- (39) Yang, S.; Zhang, H.; Hsu, S. M. Correction of Random Surface Roughness on Colloidal Probes in Measuring Adhesion. *Langmuir* **2007**, *23* (3), 1195–1202.
- (40) Monti, J. M.; McGuiggan, P. M.; Robbins, M. O. Effect of Roughness and Elasticity on Interactions between Charged Colloidal Spheres. *Langmuir* **2019**, *35* (48), 15948–15959.
- (41) Zhang, D.; Chen, X. Q.; Wang, Y.; Zhang, F. H.; Gan, Y. Relationship between Asperity-Mediated Surface Forces and Topography Alteration of Silica Microspheres Sliding on Mica, Sapphire, and Glass Substrates under Ambient Conditions: Atomic Force Microscopy and Theoretical Studies. *Langmuir* **2014**, *30* (13), 3729–3740.
- (42) Villarrubia, J. S. Algorithms for Scanned Probe Microscope Image Simulation, Surface Reconstruction, and Tip Estimation. *J. Res. Natl. Inst. Stand. Technol.* **1997**, *102* (4), 425–454.
- (43) Fujisawa, S.; Yokoyama, K.; Sugawara, Y.; Morita, S. Analysis of Experimental Load Dependence of Two-Dimensional Atomic-Scale Friction. *Phys. Rev. B - Condens. Matter Mater. Phys.* **1998**, *58* (8), 4909–4916.
- (44) Medyanik, S. N.; Liu, W. K.; Sung, I.-H.; Carpick, R. W. Predictions and Observations of Multiple Slip Modes in Atomic-Scale Friction. *Phys. Rev. Lett.* **2006**, *97* (13), 136106.
- (45) Steiner, P.; Roth, R.; Gnecco, E.; Baratoff, A.; Maier, S.; Glatzel, T.; Meyer, E. Two-Dimensional Simulation of Superlubricity on NaCl and Highly Oriented Pyrolytic Graphite. *Phys. Rev. B* **2009**, *79* (4), 45414.
- (46) Dienwiebel, M.; Pradeep, N.; Verhoeven, G. S.; Zandbergen, H. W.; Frenken, J. W. M. Model Experiments of Superlubricity of Graphite. *Surf. Sci.* **2005**, *576* (1–3), 197–211.
- (47) Dietzel, D.; Ritter, C.; Mönninghoff, T.; Fuchs, H.; Schirmeisen, A.; Schwarz, U. D. Frictional Duality Observed during Nanoparticle Sliding. *Phys. Rev. Lett.* **2008**, *101* (12), 125505.
- (48) Shen, B.; Lin, Q.; Chen, S.; Huang, Z.; Ji, Z.; Cao, A.; Zhang, Z. Double-Vacancy Controlled Friction on Graphene: The Enhancement of Atomic Pinning. *Langmuir* **2019**, *35* (40), 12898–12907.

- (49) Buzio, R.; Gerbi, A.; Barra, M.; Chiarella, F.; Gnecco, E.; Cassinese, A. Subnanometer Resolution and Enhanced Friction Contrast at the Surface of Perylene Diimide PDI8-CN 2 Thin Films in Ambient Conditions. *Langmuir* **2018**, *34* (10), 3207–3214.
- (50) Filleter, T.; Bennewitz, R. Structural and Frictional Properties of Graphene Films on SiC(0001) Studied by Atomic Force Microscopy. *Phys. Rev. B* **2010**, *81* (15), 155412.
- (51) van Wijk, M. M.; Dienwiebel, M.; Frenken, J. W. M.; Fasolino, A. Superlubric to Stick-Slip Sliding of Incommensurate Graphene Flakes on Graphite. *Phys. Rev. B* **2013**, *88* (23), 235423.
- (52) Li, B.; Yin, J.; Liu, X.; Wu, H.; Li, J.; Li, X.; Guo, W. Probing van Der Waals Interactions at Two-Dimensional Heterointerfaces. *Nat. Nanotechnol.* **2019**, *14* (6), 567–572.
- (53) Liu, Y.; Song, A.; Xu, Z.; Zong, R.; Zhang, J.; Yang, W.; Wang, R.; Hu, Y.; Luo, J.; Ma, T. Interlayer Friction and Superlubricity in Single-Crystalline Contact Enabled by Two-Dimensional Flake-Wrapped Atomic Force Microscope Tips. *ACS Nano* **2018**, *12* (8), 7638–7646.
- (54) Li, J.; Li, J.; Jiang, L.; Luo, J. Fabrication of a Graphene Layer Probe to Measure Force Interactions in Layered Heterojunctions. *Nanoscale* **2020**, *12* (9), 5435–5443.
- (55) Vazirisereshk, M. R.; Ye, H.; Ye, Z.; Otero-de-la-Roza, A.; Zhao, M.-Q.; Gao, Z.; Johnson, A. T. C.; Johnson, E. R.; Carpick, R. W.; Martini, A. Origin of Nanoscale Friction Contrast between Supported Graphene, MoS₂, and a Graphene/MoS₂ Heterostructure. *Nano Lett.* **2019**, acs.nanolett.9b02035.
- (56) Zhou, X.; Liu, Y.; Hu, X.; Fang, L.; Song, Y.; Liu, D.; Luo, J. Influence of Elastic Property on the Friction between Atomic Force Microscope Tips and 2D Materials. *Nanotechnology* **2020**, *31* (28).
- (57) Klein, H.; Pailharey, D.; Mathey, Y. Friction Force Studies on Layered Materials Using an Atomic Force Microscope. *Surf. Sci.* **1997**, *387* (1–3), 227–235.
- (58) Bilas, P.; Romana, L.; Bade, F.; Delbe, K.; Mansot, J. L. Speed and Atmosphere Influences on Nanotribological Properties of NbSe₂. *Tribol. Lett.* **2009**, *34* (1 SPEC. ISS.), 41–48.
- (59) Lantz, M.; O’Shea, S.; Welland, M.; Johnson, K. Atomic-Force-Microscope Study of Contact Area and Friction on. *Phys. Rev. B - Condens. Matter Mater. Phys.* **1997**, *55* (16), 10776–10785.

Sliding friction and superlubricity of colloidal AFM probes coated by tribo-induced graphitic transfer layers

Renato Buzio^{*,†}, Andrea Gerbi[†], Cristina Bernini[†], Luca Repetto[‡], Andrea Vanossi^{§,⊥}

[†] CNR-SPIN, C.so F.M. Perrone 24, 16152 Genova, Italy

[‡] Dipartimento di Fisica, Università degli Studi di Genova, Via Dodecaneso 33, 16146 Genova, Italy

[§] CNR-IOM Democritos National Simulation Center, Via Bonomea 265, 34136 Trieste, Italy

[⊥] International School for Advanced Studies (SISSA), Via Bonomea 265, 34136 Trieste, Italy

Supplementary Information

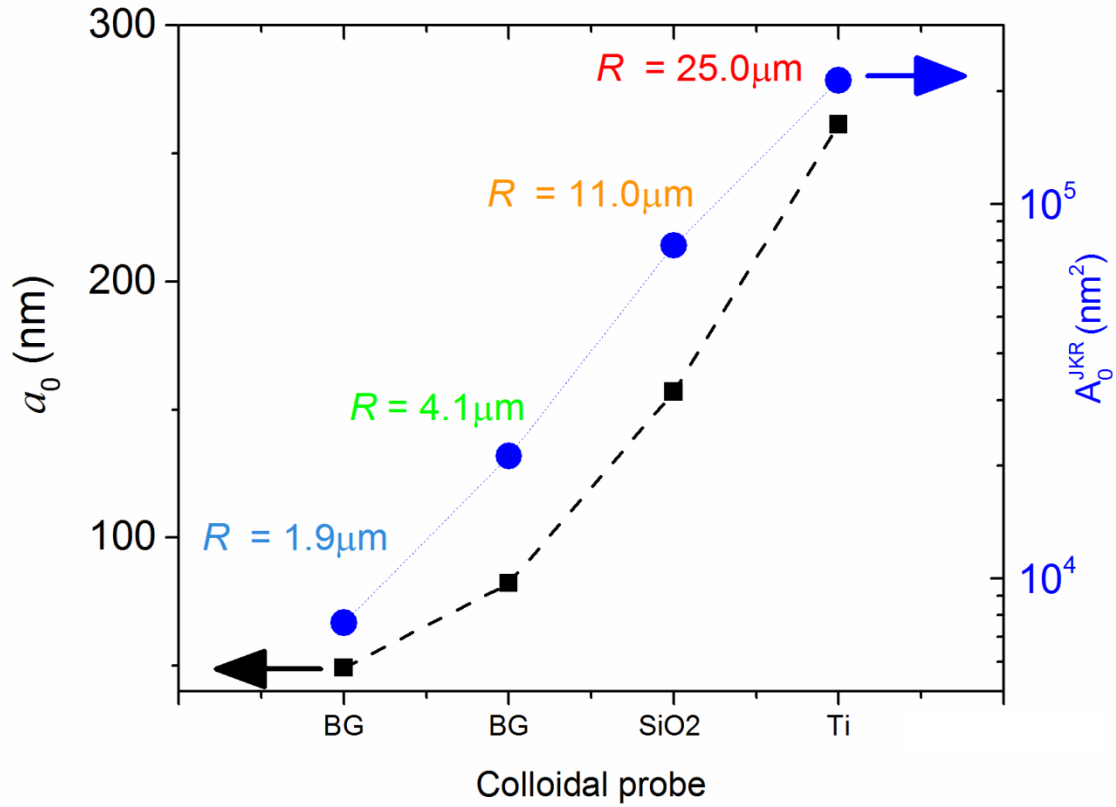


Figure S1. Zero-load contact radius a_0 and contact area A_0^{JKR} evaluated using the JKR theory, for ideally smooth beads with the same size of those used in the present study (material parameters: Young modulus E (BG) = 64GPa, Poisson ratio ν (BG) = 0.2; E (SiO₂) = 70GPa and ν (SiO₂) = 0.2; E (Ti) = 100GPa and ν (Ti) = 0.35; E (HOPG) = 30GPa and ν (HOPG) = 0.24; interfacial energy γ = 50mJ/m²). See also Ref. [12] of the main text for calculation details.

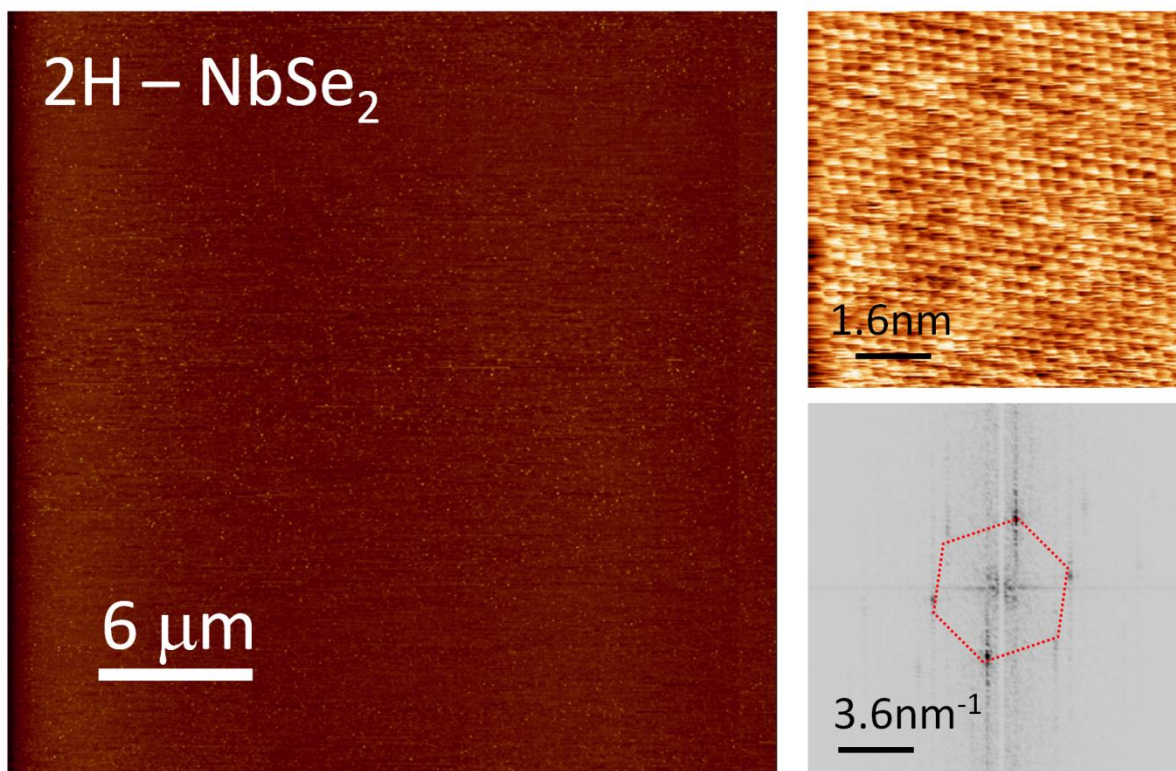
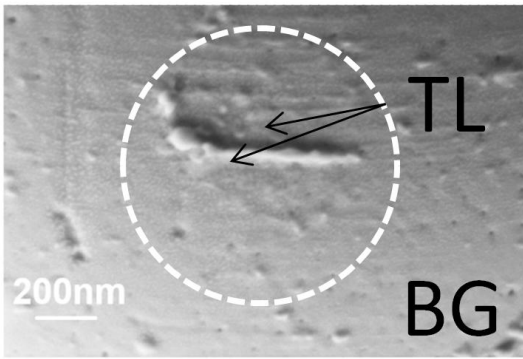
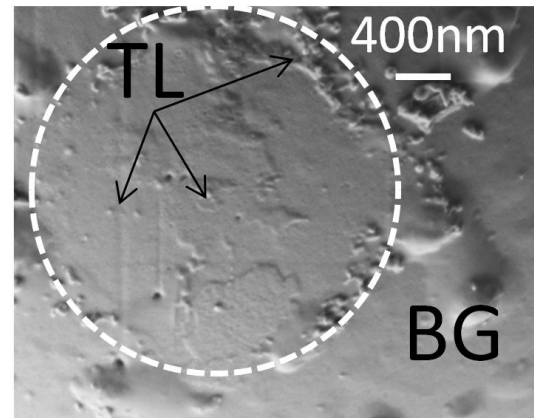


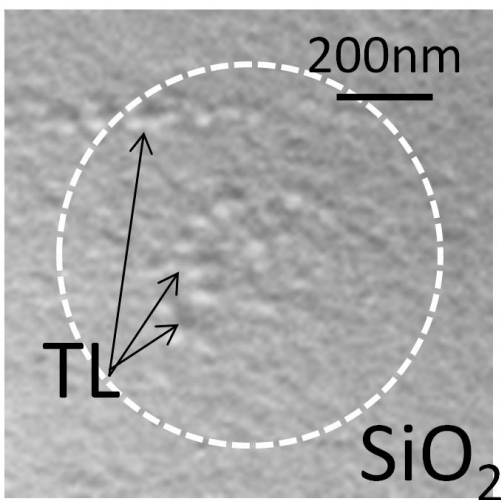
Figure S2. (Left) Typical AFM topography of the laboratory-grown 2H-NbSe₂ single-crystal sample: it shows an atomically-flat region, extending tens of micrometers in lateral size without atomic steps. (Right) Raw atomic-scale STM topography acquired on the same sample (Omicron Nanotechnology LT-STM, T = 80K). The hexagonal symmetry of the surface lattice is clearly resolved in the related 2D Fast Fourier Transform FFT map.



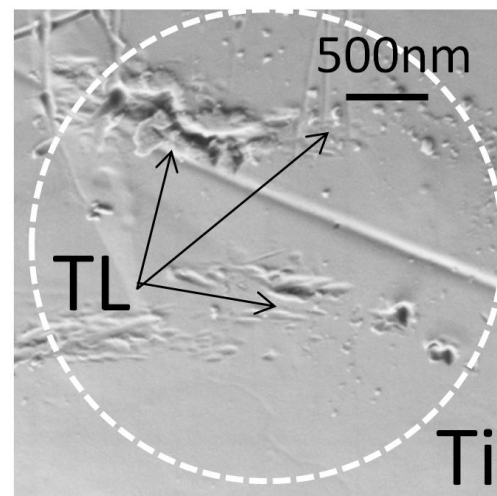
$R = 1.9 \mu\text{m}$



$R = 4.1 \mu\text{m}$

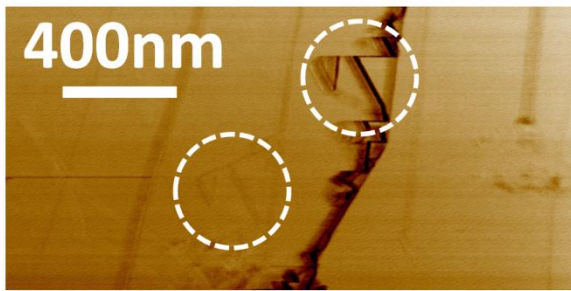


$R = 11.0 \mu\text{m}$

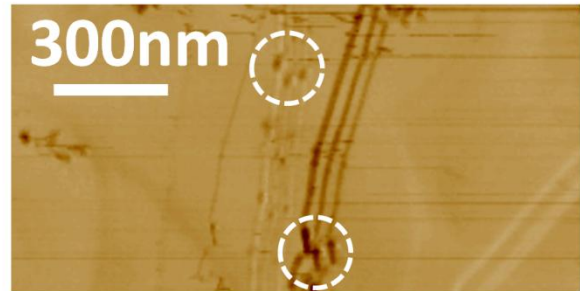


$R = 25.0 \mu\text{m}$

Figure S3. SEM micrographs of the contact area of each bead. They confirm the presence of the tribotransferred flakes. Micrographs agree with AFM topographies of Figure 3 (main text).



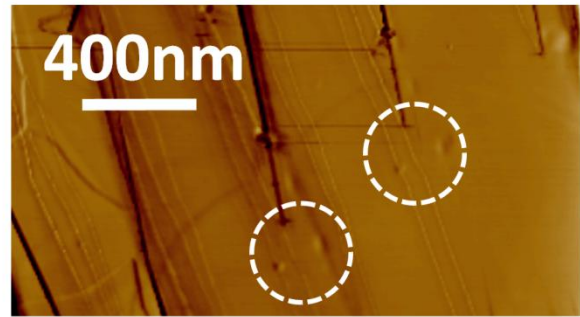
$R = 1.9 \mu\text{m}$



$R = 4.1 \mu\text{m}$



$R = 11.0 \mu\text{m}$



$R = 25.0 \mu\text{m}$

Figure S4. Multiple-tip effects originated by a rough TL. Examples of multiple-tip patterns in lateral force maps acquired with the TL/HOPG contact. Besides such patterns, multiple step edges occur.

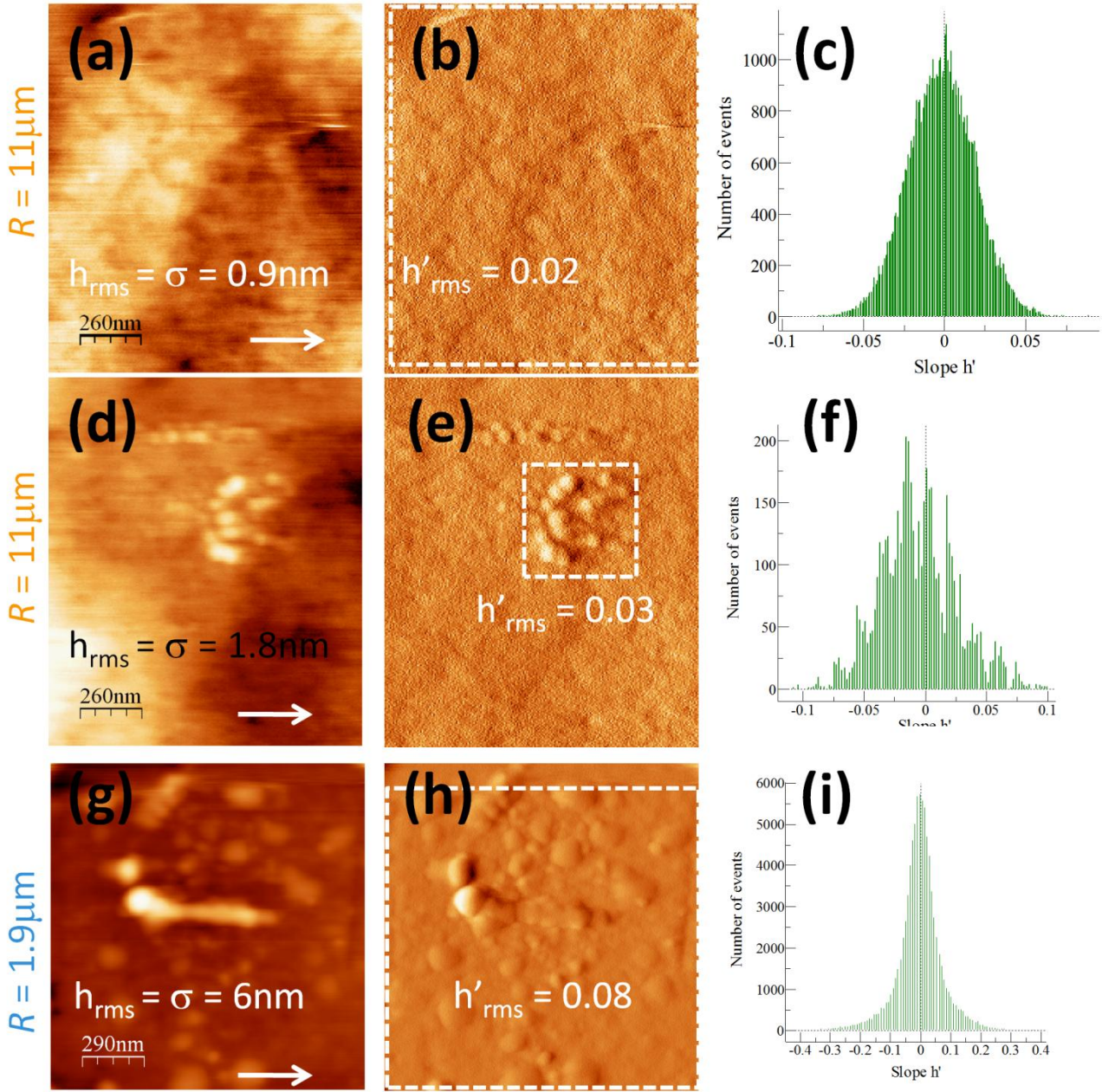


Figure S5. Evaluation of the average local slope h'_{rms} from AFM topographies. (a-c). Pristine morphology of the bead with $R = 11\mu\text{m}$. From the topography map h in (a), the map of local slopes h' (along the white arrow direction) is obtained by finite differences (in (b)). Root mean square values are calculated for both maps. In (c) is the histogram of h' . (d-f) the same as above, but for the bead with $R = 11\mu\text{m}$ after the TL formation. (g-i) the same as in (d-f), for the bead with $R = 1.9\mu\text{m}$ and after TL formation. **Evaluation of the critical load N_C .** According to Pastewka et al. Appl. Phys. Lett. 2016, 108 (22), in the nonadhesive hard-wall repulsion limit ($1/\kappa = 0.5$), with $E^* = 30\text{GPa}$ (HOPG-dominated interfacial deformation), and $R = 1.9\mu\text{m}$, $h'_{rms} = 0.08$ one gets $N_C \sim 120\mu\text{N}$. Also, for $R = 11\mu\text{m}$ and $h'_{rms} = 0.03$, one has $N_C \sim 210\mu\text{N}$. Hence $F_N/N_C \sim 5 - 8 \times 10^{-4}$ at $F_N = 100\text{nN}$ and $F_N/N_C < 1 \times 10^{-4}$ for $F_N \sim 10\text{nN}$.

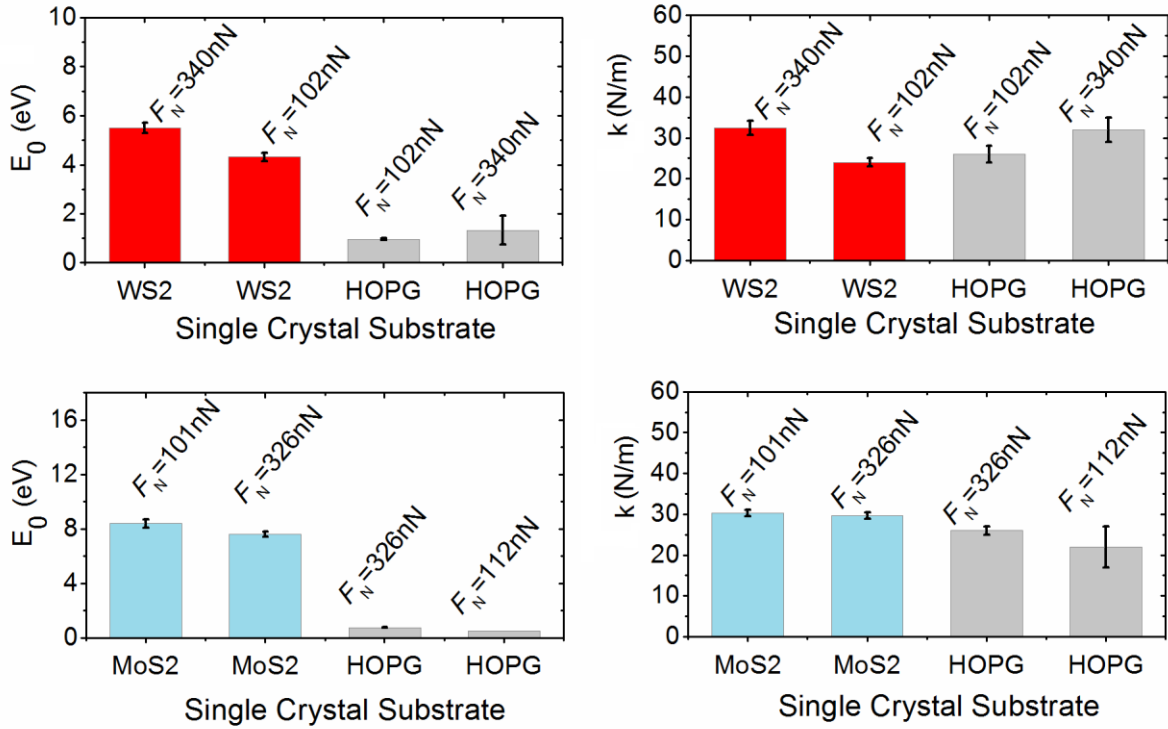


Figure S6. Evaluation of potential corrugation E_0 and contact stiffness k for sliding hetero-junctions, formed by contacting the tribo-induced graphitic TL with transition metal dichalcogenides.

Top graphs: E_0 and k_{eff} for the TL/WS₂ hetero-junction (red bars) are compared with the same quantities evaluated for the TL/HOPG homo-junction (grey bars; this is the superlubric starting condition, see main text). Two values of F_N are taken into account (102nN and 340nN). One notes that $k(\text{TL}/\text{WS}_2) \sim k(\text{TL}/\text{HOPG})$ whereas $E_0(\text{TL}/\text{WS}_2) \sim 5 \times E_0(\text{TL}/\text{HOPG})$, that implies $\eta(\text{TL}/\text{WS}_2) \sim 3 \times \eta(\text{TL}/\text{HOPG}) \sim 6$.

Bottom graphs: E_0 and k_{eff} for the TL/MoS₂ hetero-junction (light blue bars) are compared with the same quantities evaluated for the TL/HOPG homo-junction (grey bars; superlubric starting condition). In this case $k(\text{TL}/\text{MoS}_2) \sim k(\text{TL}/\text{HOPG})$ whereas $E_0(\text{TL}/\text{MoS}_2) \sim 12 \times E_0(\text{TL}/\text{HOPG})$, and $\eta(\text{TL}/\text{MoS}_2) \sim 4 \times \eta(\text{TL}/\text{HOPG}) \sim 8$.